Journal of Energy Chemistry 49 (2020) 224–232

Contents lists available at ScienceDirect

Journal of Energy Chemistry

journal homepage: www.elsevier.com/locate/jechem

http://www.journals.elsevier.com/journal-of-energy-chemistry/

Boosting the electrochemical performance and reliability of conducting polymer microelectrode via intermediate graphene for on-chip asymmetric micro-supercapacitor

Muhammad Tahir, Liang He, Wei Yang, Xufeng Hong, Waqas Ali Haider, Hui Tang, Zhe Zhu, Kwadwo Asare Owusu, Liqiang Mai*

State Key Laboratory of Advanced Technology for Materials Synthesis and Processing, Wuhan University of Technology, Wuhan 430070, Hubei, China

ARTICLE INFO

Article history:
Received 9 January 2020
Revised 20 February 2020
Accepted 20 February 2020
Available online 4 March 2020

Keywords:
Electrochemical polymerization
Nucleation
Asymmetric microsupercapacitors

ABSTRACT

High-performance anode is hurdle for on-chip planar microsupercapacitor (MSC). Polypyrrole (PPy) is a highly attractive pseudocapacitive material, but its low cycling stability, and low adhesion with current collector hinder its practicability. Herein we propose one-prong generic strategy to boost the cycling stability of PPy. For our strategy, the electrochemical deposition of multilayered reduced graphene oxide (rGO) on micropatterned Au is utilized, and the resultant rGO@Au pattern is then used for growing highly porous PPy nanostructures by facile electrochemical polymerization. The fabricated PPy anode on rGO@Au has quasi rectangular cyclic voltammetry curves up to -0.7 V and exceptional cycling stability, retaining 82% of capacitance after 10,000 charge/discharge cycles in 2 M KCl electrolyte. The outstanding reliability of PPy on rGO@Au is due to the flexibility of rGO, accommodating structural pulverization and providing a promising background for the nucleation of highly porous nanostructure. Further, an all-polymer based asymmetric aqueous MSC (AMSC) is constructed with PPy anode and PEDOT cathode, which exhibited excellent electrochemical performance compared with conventional symmetric MSCs based on conducting polymers. The constructed AMSC delivered a maximum areal capacitance of 15.9 mF cm^{-2} (99.3 F cm^{-3}), high specific energy and power densities of 4.3 μWh cm^{-2} (27.03 mWh cm^{-3}) and 0.36 W cm^{-2} (0.68 W cm^{-3}) at 1.4 V, respectively. The enhanced electrochemical performances can be illustrated by nucleation mechanism, in which surface topology of rGO generates a promising background for nucleation and electrochemical growth of nanoporous pseudocapacitive conducting polymers with superior interfacial contact and improved surface area.

1. Introduction

The constantly-growing demand for portable electronics has provoked significant attention regarding miniaturization of high-performance planar micro energy storage device [1–4]. Microsupercapacitor (MSC) is a predominantly fascinating microelectrochemical power source owing to its tiny size, fine structure, comparatively high power, long-term cycling life, and high compatibility for integration with multi-functional chips and microsystems [5–8]. Despite enormous progresses have been achieved in MSC through evolution of microfabrication techniques such as lithography, screen printing and laser scribing, its energy density is still inadequate due to its low operating voltage and low specific capacitance [9–12]. Recently nickel foam and carbon cloth are widely applied as 3D current collectors for high mass loading of active materials, however, they are quite massive to be compatible with microchips. To achieve portable electronic devices with integrated energy-storage components, it is essential to incorporate MSC into microsystem, and the interdigital planar MSC is a highly competitive candidate, because of its short ion diffusion path, high stability, excellent kinetic performance and facile integration into electronic circuits [13,14].

Currently a lot of efforts have been utilized in developing carbon and carbon/metal oxide composite through various construction techniques [15–18]. Activated carbon-based MSCs for instance carbide compound derived carbon [19], carbon nano-onion [20], thermally activated carbon [21] and carbon nanotube (CNT)

* Corresponding author.
E-mail address: mlq518@whut.edu.cn (L. Mai).

https://doi.org/10.1016/j.jechem.2020.02.036

[22] electrodes are obtained by photolithography and conventional methods including sputtering, inkjet printing, electrophoretic deposition and spray coating. Further, 3D MSCs based on 1D CNTs or 2D graphene are fabricated *via* chemical vapor deposition [23,24]. Recently, reduced graphene oxide (rGO) is attracting much attention in energy storage applications owing to its large surface area, high theoretical capacity, high electrical conductivity, and great functionality [25]. For instance, Gao et al. used laser reduction of GO film to fabricate integrated rGO MSC [26]. EI-Kady et al. studied rGO MSC based on GO coated digital video disk (DVD) through laser scribe technique [7]. Wu et al. fabricated rGO MSC using photolithography, followed by oxygen plasma etching to fabricate rGO micropatterns [27]. The charge storage mechanism of carbonaceous materials is electrical double layer capacitance (EDLC), so this kind of MSCs will deliver low capacitance. Therefore, to improve the capacitance of MSC, pseudocapacitive materials like transition metal oxides/hydroxides (MnO_2, RuO_2, $Ni(OH)_2$, $Co(OH)_2$) [28,29] and conducting polymers (PPy, PEDOT, PANI) [30–32] are investigated due to their reversible redox reaction on/into their surfaces [33–35].

One of the drawbacks of pseudocapacitive materials is their limited cycling performance. For on-chip interdigital planar MSCs, the anode is a critical issue. Activated carbon, graphene, iron compounds (Fe_2O_3, Fe_3O_4, FeOOH) and polypyrrole (PPy) are reported as anodes in supercapacitors [16,28]. PPy is a highly attractive pseudocapacitive material because of suitable voltage window, low toxicity, facile fabrication process, high electrical conductivity and low cost [36–39]. However, the low cycling stability of PPy (<50% after 1000 cycles), relatively high stiffness and low adhesion with substrate hinder its wide applications in energy storage [36,40,41]. Upon oxidation, the generation of charged nitrogen groups (polarons) on PPy chain, and the movement of counterions from electrolyte to PPy matrix cause the matrix to expand. During reduction, counterions drawn-out back to electrolyte to conserve the charge neutrality, causing PPy matrix to shrink. The continuous expansion and shrink make structural pulverization and activity loss of PPy [42,43]. Secondly the adhesion of PPy film with current collector is another challenge. During electrochemical reaction, the PPy film always peel off from the current collector due to its low adhesion nature and offers high resistance and instability.

Recently many efforts have been dedicated to enhancing the cycling stability of PPy-based electrodes for energy storage devices. It is demonstrated that the flexible substrate such as rGO and CNT will accommodate volumetric change of electrode during cycling and suppress structural pulverization of PPy [44–48]. Also the surface topology of rGO provides a promising background in lieu of the nucleation besides the electrochemical growth of nanoporous pseudocapacitive conducting polymers revealing superior interfacial contact and large surface area. We recently reported PEDOT-CNT based MSCs, showing ideal capacitive performance with polymer gel electrolytes [49]. However, the specific capacitance and energy of these MSCs need to be improved.

Herein, we reported nanostructured PPy microelectrode anchored on electrochemically deposited multilayered rGO@Au as an anode, which has excellent electrochemical performance in aqueous electrolyte, retaining 82% of the capacitance after 10,000 charge/discharge cycles. The buffering effect between these two constituents (PPy and graphene) is oppressed in which rGO offers not only a superficial charge transport, nevertheless a mechanical support in improving cycling stability of microelectrode. Further, an asymmetric MSC (AMSC) was fabricated using PPy@rGO anode and PEDOT@rGO cathode which delivered high areal and volumetric specific capacitances of 15.9 mF cm^{-2} and 99.3 F cm^{-3} respectively, with a wide operating voltage window of 1.4 V in 2 M aqueous KCl electrolyte. Further the all polymer-based AMSC showed a capacitance retention of 79% after 5000 cycles at a high current density of 5 mA cm^{-2}.

2. Experimental

2.1. Fabrication of rGO@Au current collector

Microfabrication process of PPy@rGO//PEDOT@rGO-AMSC is schematically shown in Figs. 1 and S1.

The micropatterned photoresist (PR1-9000A) was prepared on a Si/SiO_2 wafer as reported in our previous work. Briefly, 1 × 1 cm Si/SiO_2 wafer was cleaned with ultrasonication in isopropanol alcohol, ethanol, acetone and deionized (DI) water in sequence. The PR1-9000A layer was spun coated on wafer by two consecutive steps (500 rpm,10 s; 5000 rpm, 40 s). The micropatterned photoresist was obtained after exposing the sample to UV light through a photomask and developing in RD-6 developer. Then, a Cr/Au (5/50 nm) layer was deposited on the sample by thermal evaporation (the dimensions and area of Cr/Au micropattern are shown in Fig. S2). For the deposition of multi layered graphene, 0.5 mL of 0.05 molar sodium sulfate solution was mixed with GO solution (2 mg/mL, 20 ml). The anodic deposition was performed at a current density of 2 mA cm^{-2} for 100 s, and the deposition step was repeated for two times. After drying, the sample was soaked in acetone for 6 h, and the multilayered rGO@Au interdigital micro current collectors were fabricated after lift-off.

2.2. Fabrication of PPy @rGO anode

PPy was electrochemically deposited on rGO@Au micropatterns by three-electrode system. For the preparation of electrolyte, pyrrole (100 µL) was mixed with deionized (DI) water (20 mL) by continuous stirring. Then concentrated sulphuric acid (50 µL, 98% H_2SO_4) was added dropwise in above solution. Afterward, 0.01 M sodium dodecyle sulfate (SDS) was added into the solution followed by stirring for 30 min. Before deposition, the solution was ultrasonicated for 2 min until a transparent solution without suspended particles was obtained. The cyclic voltammetry (CV) deposition was performed at a scan rate of 10 mV s^{-1} for 7 cycles in the voltage range of 0.7–0.75 V. The anionic surfactant of SDS lowers the oxidation potential and is favorable for the deposition of highly porous PPy on rGO. Finally, the sample was washed by DI water thoroughly to eliminate unreacted polymer and dried under vacuum at 60 °C for one hour.

2.3. Preparation of PEDOT@rGO cathode

PEDOT nanospheres were deposited on the other side of rGO@Au micropatterns by electrochemical deposition. The electrolyte solution was prepared consistent with our previous work with a little modification [49]. Generally, 10 mM of 98% H_2SO_4 was added dropwise in 20 mL of DI water, followed by addition of 10 mM ethylenedioxythiophene (EDOT) monomers and SDS (10 mM). Afterward, the mixture was stirred for 4 h and then ultrasonicated for 5 min prior to deposition. The deposition was conducted at a constant potential of 0.9 V for 250 s.

2.4. Material characterization

The structure and surface morphology of prepared samples were observed by a field emission scanning electron microscope (FE-SEM, JSM-7100F). A TEM-1400-P transmission electron microscope (TEM) was employed to study the submicron details of microelectrodes. A Renishaw RM-1000 laser Raman microscopy system was used to collect Raman spectra of samples. X-ray photoelectron spectroscope (XPS) spectra of samples were collected

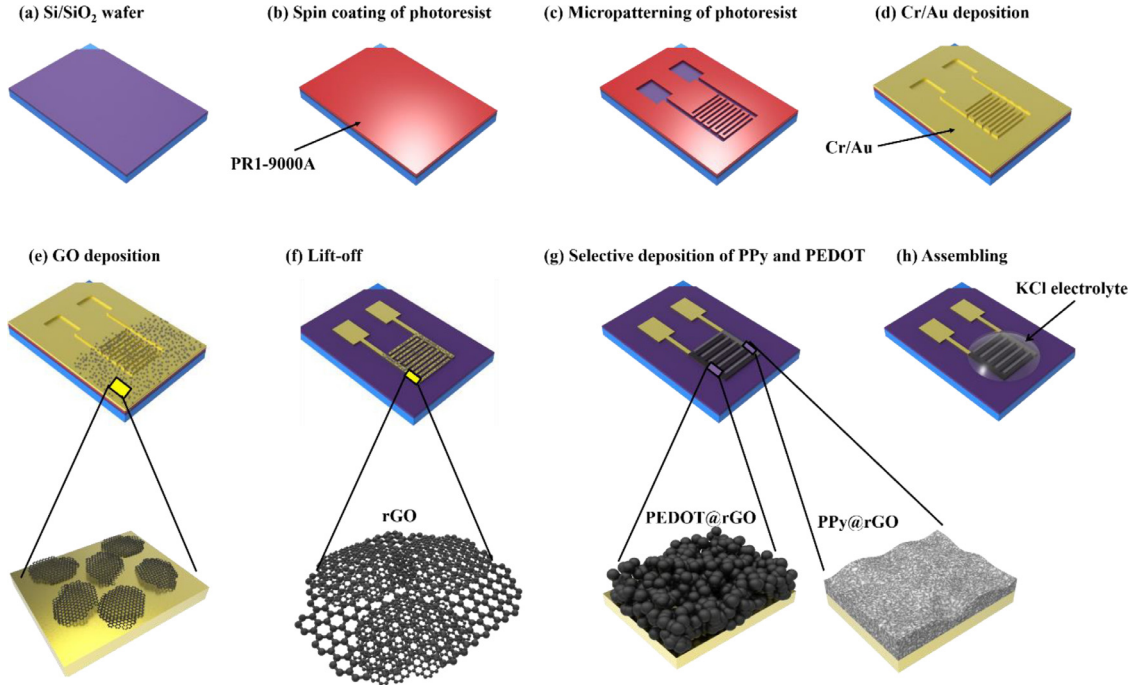

Fig. 1. (a–h) Schematic view of microfabrication process of PPy@rGO//PEDOT@rGO-AMSC.

using a VG Multilab 2000. The thicknesses of microelectrodes were measured by atomic force microscope (AFM, Burker NT-MDT). Electrochemical tests were performed using CHI-760 electrochemical work station.

3. Results and discussion

Fig. 2(a) shows the optical microscopic image of rGO@Au micropatterns. The layered graphene is uniformly deposited on Au current collectors and tightly bonded with Au even after lift-off process in acetone with ultrasonication. A fine micropatterned rGO@Au is obtained after lift-off. Fig. 2(b, c) display the SEM images of interdigital layered rGO microelectrodes on Cr/Au. Some wrinkles are observed on rGO film and are favorable for the penetration of electrolyte ions into the interior of rGO micropatterns and enhancement of the surface area. The rGO film has positive effects on the uniform deposition of pseudocapacitive material. The versatile nature of rGO regarding chemical functionality and electrical conductivity facilitates the homogeneous nucleation/growth of pseudocapacitive conductive polymer. The rGO film consists of numerous surface-steps and interfaces, which improves the adhesion of polymer with microchannel resulting in low contact resistance and high electrochemical performance. Fig. 2(d) displays the optical microscopic image of PPy@rGO anode (grey) and PEDOT@rGO cathode (black). The short-time deposition prevents the spreading of polymers to obtain fine micropatterns. The morphologies of electrochemically deposited PPy and PEDOT on rGO and Au are displayed in Fig. 2(e, f) and S3 respectively. The mesoporous morphology of PPy is optimal for the rapid transport of electrolyte ions deep into PPy matrix. Additionally, the flexibility of rGO prevents the structural pulverization of PPy mesoporous network. Contrary to this, PPy electrodeposited on Au micropatterns shows dense and low porous popcorn type structures with low adhesion with current collectors, causing low conductivity and poor cycling performance (Fig. S3e, f).

Further, TEM characterization was performed for the morphological analysis of PPy@rGO, and the results are displayed in Fig. 2(h). Electrochemically polymerized PPy on rGO shows uniformly distributed dark regions, specifying the homogeneous distribution of PPy on rGO nanosheets. The inset shows the very thin 2D nanosheets of electrochemically deposited rGO.

The thicknesses of rGO and conducting polymers (PPy@rGO, PEDOT@rGO) films were measured by AFM in the tapping mode. The maximum thickness of rGO film for three consecutive cycles deposition was 22.7 nm, whereas the least thickness of a single sheet was 1 nm (Fig. S4). The average thicknesses of PPy@rGO and PEDOT@rGO microelectrodes were found to be 1.4 (7 CV cycles) and 1.8 μm (deposition time is 250 s) respectively (Fig. S5a, b).

Raman spectra of GO, rGO, PPy@Au and PPy@rGO were recorded and displayed in Fig. 2(i). Two typical peaks positioned at 1349 and 1579 cm^{-1} resemble D and G bands of sp^2 carbon atoms in the 2D hexagonal matrix. The intensity ratio of D to G represents the degree of disordered graphite. I_D/I_G of rGO is 1.2 compared with 1.0 of GO, revealing the higher disorder in electrochemically rGO. For pristine PPy, the peaks positioned at 1379 and 1578 cm^{-1} specify corresponding ring stretching of oxidized PPy and C=C backbone stretching mode of PPy respectively. Likewise, three consecutive peaks at 927, 965 and 1061 cm^{-1} correspond to the deformation of bipolaron rings and bending vibration of symmetric C-H plane bending vibrations [50,51]. The value of I_D/I_G for PPy is 0.8. The Raman spectrum of PPy@rGO displays the bands of PPy and rGO, and its I_D/I_G increases to 0.96 showing the higher degree of graphitization in PPy@rGO matrix. The shift of G band from 1602 to 1580 cm^{-1} confirms the complete reduction of GO to rGO during electrochemical deposition [52].

To confirm the presence of functional groups in the PPy@rGO, XPS measurement was conducted. Fig. S6(a) illustrates the comparison of deconvoluted C 1*s* and O 1*s* spectra of PPy and PPy@rGO microelectrodes. The C 1*s* core-level spectrum of PPy@rGO microelectrode can be tailored into 5 constituent peaks at binding energies of 284.5, 285, 285.6, 286.9, and 289.0 eV, belong to sp^2, sp^3 hybridized carbon, C-N, C=O, and COOH, respectively [51]. Whereas, for PPy@Au microelectrode, the sp^3 hybridized carbon peak, C=O peak and COOH peaks are absent which shows the

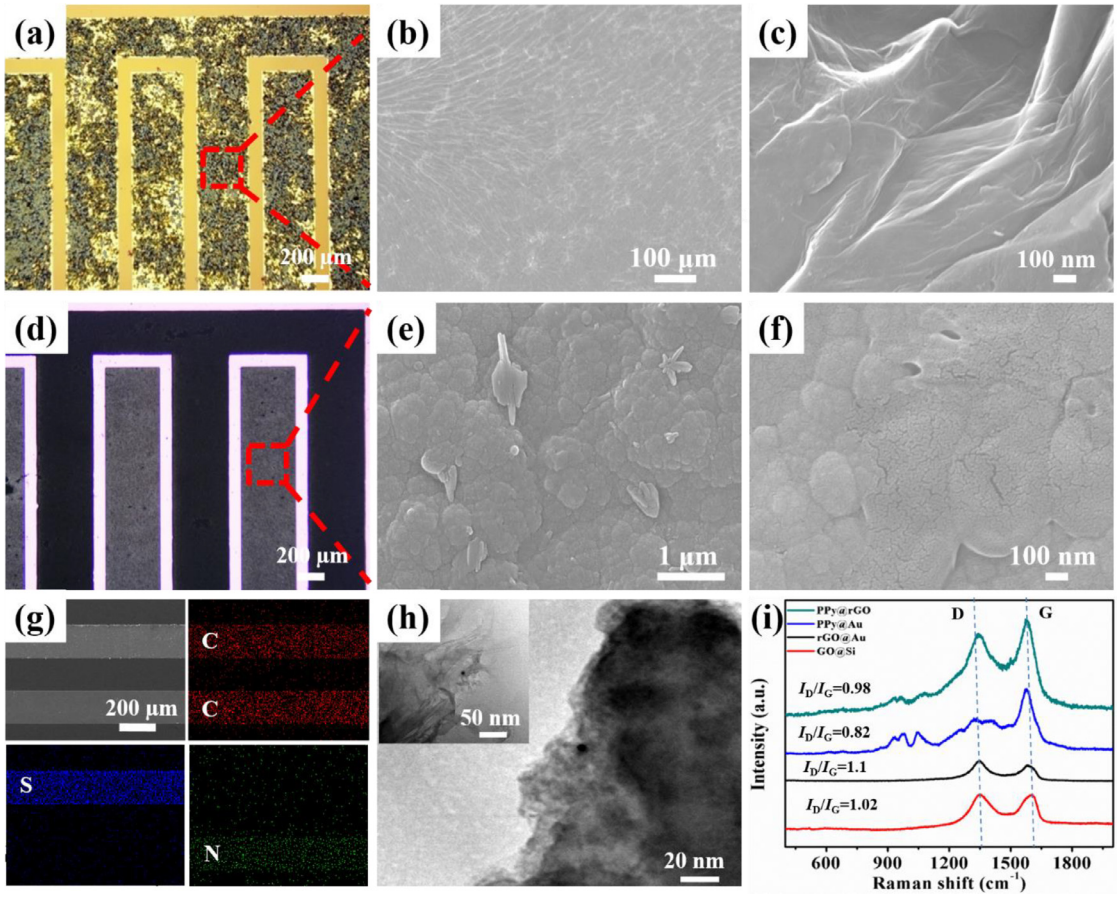

Fig. 2. Material characterization results. (a) Optical image of rGO coated Cr/Au current collectors on Si/SiO_2 substrate. (b, c) Low- and high-resolution SEM images of electrochemically deposited rGO on Cr/Au current collectors. (d) Optical image of the fabricated microelectrodes in AMSC. (e, f) SEM images of electrochemically deposited PPy@rGO. (g) EDS elemental mapping of C, S, N elements in PPy@rGO and PEDOT@rGO microelectrodes. (h) TEM images of PPy@rGO (the inset shows the rGO). (i) Raman spectra of PPy@rGO, PPy@Au, rGO and GO films.

introduction of carbonyl (C=O) and carboxyl (COOH) functional groups in PPy@rGO microelectrode. Similarly, Figure S6(b) displays the O 1*s* spectra of PPy@rGO revealing carbonyl (C=O) and carboxyl (-COOH) functional groups at binding energies of 531 and 533.9 eV in PPy@rGO microelectrode, respectively [53].

3.1. Electrochemical measurements

3.1.1. Electrochemical characterization of PPy @rGO and PEDOT@rGO

To appraise the electrochemical activity of PPy@rGO as an anode of MSC, electrochemical test was performed in a three-electrode system using PPy@rGO (working electrode), Pt (counter electrode) and SCE (reference electrode) in 2 M KCl electrolyte. Fig. 3(a) displays the cyclic voltammetry (CV) curves of PPy@Au and PPy@rGO microelectrodes at a scan rate of 20 mV s^{-1}. The CV curve of PPy@rGO shows a quasi-rectangular shape up to 0.7 V, signifying that the capacitance of PPy@rGO microelectrode is primarily double layer capacitance and slight surface redox reactions. This is analogous with literature [48,49]. The CV of PPy@Au is skewed left and has no capacitance in a region between −0.45 to −0.7 V. As expected, the PPy@rGO microelectrode displayed significantly larger current than that of PPy@Au microelectrode, owing to the enhanced surface area of nano porous PPy anchored on electrochemically deposited rGO with higher electrical conductivity. Fig. 3(b and c) shows the CV curves of PPy@rGO anode at diverse scan rates (2–100 mV s^{-1}). The quasi-rectangular shape of CV curves even at 100 mV s^{-1} and linear change in current with scan rate show a typical pseudocapacitive mechanism and excellent rate capability of electrode respectively. The charge/discharge curves of PPy@rGO microelectrode at various current densities (0.25 to 2 mA cm^{-2}) are displayed in Fig. 3(d). The thin layered active material (~1.45 μm) delivers an areal capacitance of 43.4 mF cm^{-2} (at a current density of 0.25 mA cm^{-2}) maintaining 77.9% of the capacitance at high current density of 2 mA cm^{-2}. The excellent rate capability is attributed to the high porosity, and high electrical conductivity of the PPy nonporous network anchored on layered rGO.

To better understand the enhanced electrochemical performances of PPy@rGO microelectrode, the resistance and charge transfer mechanism at the electrode-electrolyte interface of PPy@rGO and PPy@Au microelectrodes, electrochemical impedance spectroscopy (EIS) test is performed at open-circuit potential. Fig. 3(e) illustrates the Nyquist plots of PPy@rGO and PPy@Au microelectrodes. Both the plots contain two parts, semicircles in high frequency region and slope along vertical Y-axis respectively. The inherent material resistance, electrolyte ionic resistance and electrode-electrolyte contact resistance (R_s) are obtained from the intercept of real values (Z') at the high frequency regions. The charge transfer resistance (R_{ct}) is obtained from the semicircle at high frequency region, corresponds to the resistance during electron transfer at the electrode-electrolyte interface. An analysis of the Nyquist plots using corresponding circuits shows that the PPy@rGO offers low R_s (5.8 Ω) and R_{ct} (480 Ω) compared with large values of R_s (20.4 Ω) and R_{ct} (1705 Ω) for PPy@Au microelectrode. The low R_s and R_{ct} values of PPy@rGO microelectrode are attributed to the strong adhesion of PPy with Au *via* intermediate rGO to lower contact resistance and good ion diffusion kinet-

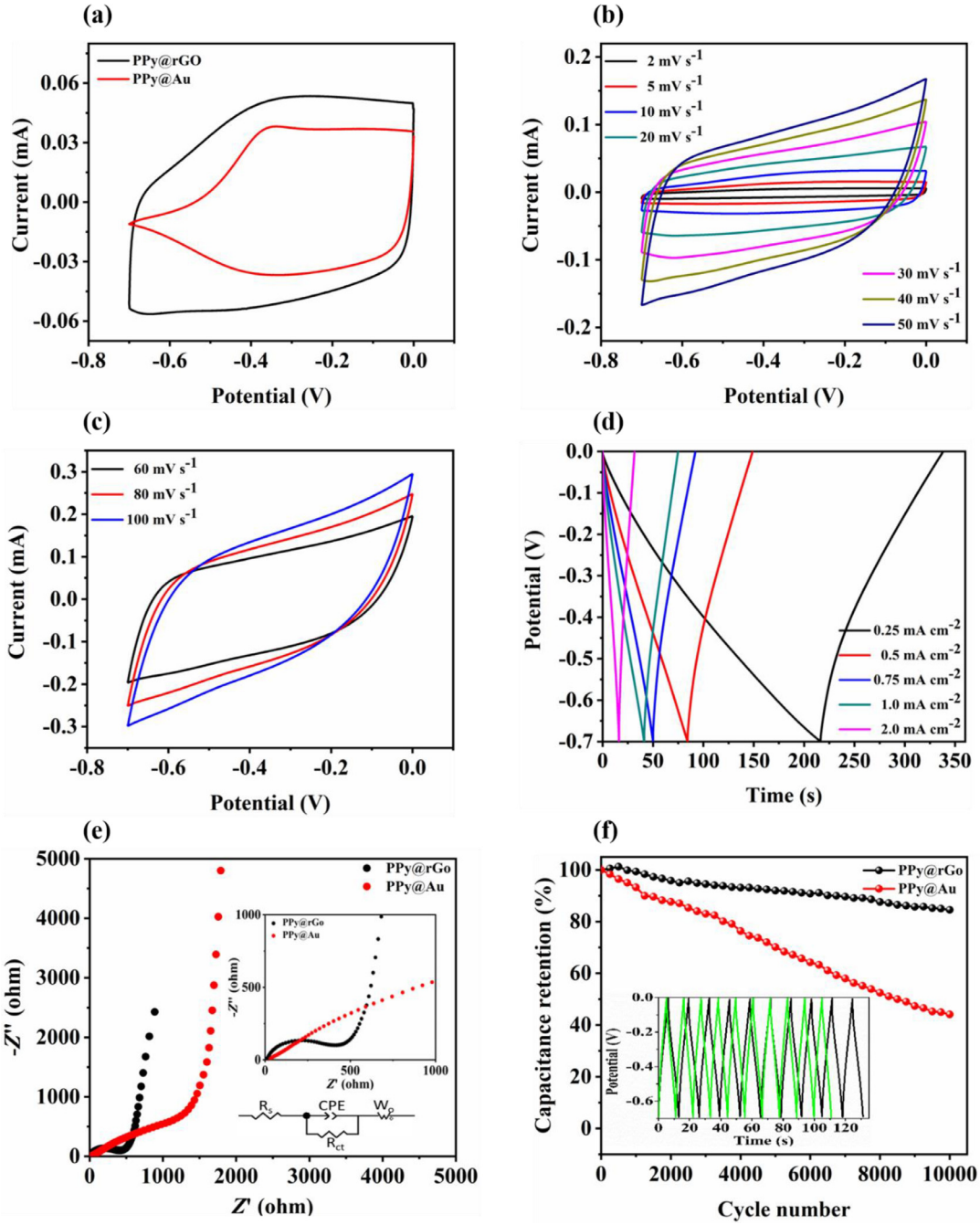

Fig. 3. (a) CV curves of PPy@Au and PPy@rGO microelectrodes at a constant scan rate of 20 mV s^{-1}. (b, c) CV curves of PPy@rGO microelectrode at different scan rates from 2 to 100 mV s^{-1} in 2 M KCl electrolyte. (d) GCD curves of PPy@rGO microelectrode at different current densities from 0.25 to 2 mA cm^{-2}. (e) EIS curves of PPy@rGO and PPy@Au microelectrodes at the frequency range of 10^{-2}–10^{5} Hz. The inset shows the results at high frequency region and equivalent circuit. (f) Long-term cycling stability of PPy@rGO and PPy@Au microelectrodes up to 10,000 GCD cycles. The inset shows the GCD curves of PPy@rGO microelectrode at initial 10 cycles (black) and last 10 cycles (green).

ics of porous PPy deposited on rGO respectively. The decreased R_{ct} suggests that the PPy@rGO facilitates fast diffusion of electrolyte ions, advantageous to the long-term stability of the anode. Fig. S7(a) shows the IR drop from GCD curves of both microelectrodes (at a current density of 0.5 mA cm^{-2}). The PPy@rGO has a small IR drop (0.02 V) compared with a high IR drop of PPy@Au microelectrode (0.23 V) which also shows the enhanced conductivity of PPy@rGO microelectrode. One of the most important electrochemical performance for conducting polymers-based energy storage devices is their cycling stability. At ambient condition, PPy suffers a poor cycling stability even less than 50% retention is obtained after few thousand cycles. Fig. 3(f) shows the cycling performance of PPy@rGO and PPy@Au microelectrodes respectively, and the inset shows the comparison of initial 10 and last 10 charge/discharge cycles. PPy@rGO microelectrode exhibits an exceptional stability in aqueous electrolyte retaining 86% of the capacitance after 10,000 charge/discharge cycles at a high current density of 10 mA cm^{-2}. Whereas, for PPy@Au microelectrode, only 40% of the capacitance

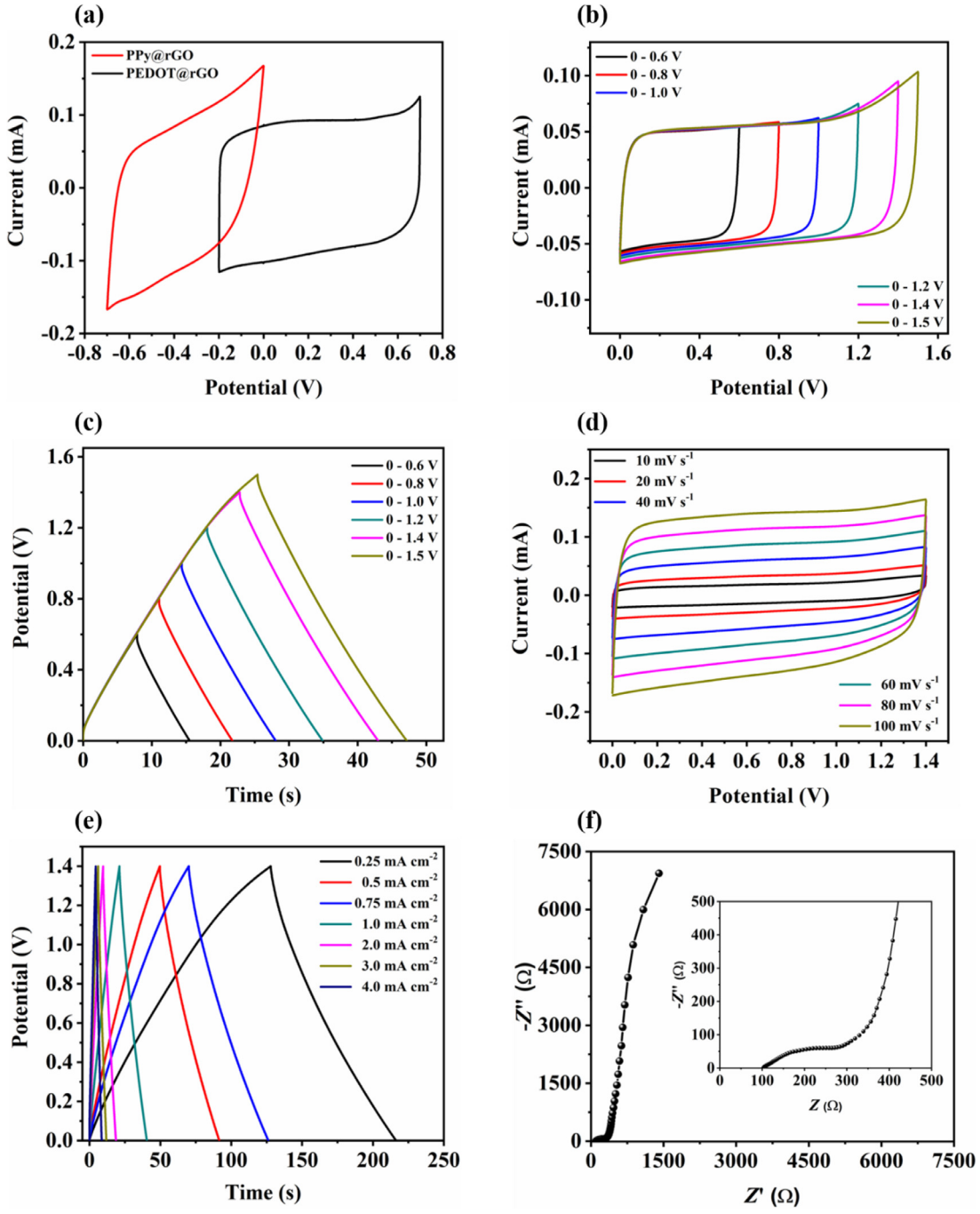

Fig. 4. Electrochemical performance of the fabricated AMSC. (a) CV curves of PPy@rGO and PEDOT@rGO microelectrodes in three-electrode system at a scan rate of 40 mV s^{-1}. (b) CV curves of fabricated AMSC at different voltage windows from 0.6 to 1.5 V at the scan rate of 30 mV s^{-1}. (c) GCD curves of AMSC sketched over different voltages from 0.6 to 1.5 V at a constant current density of 1 mA cm^{-2}. (d) CV curves of the fabricated AMSC at different scan rates from 10 to 100 mV s^{-1}. (e) GCD curves at different current densities from 0.25 to 4 mA cm^{-2} and a constant voltage of 1.4 V. (f) EIS curve of the fabricated aqueous AMSC, and the inset shows its zoom view at high frequency region.

remains after 10,000 cycles, and the film is always not stable and peeled off from current collectors within several hundreds of cycles.

To understand the phenomenon of enhanced cycling stability of PPy@rGO, the SEM images of microelectrodes before and after cycling were recorded. It is observed that PPy nanonetwork anchored on rGO has no significant cracks and also the nanonetwork microelectrode is highly stable after cycling. PPy film deposited on Au has many cracks on its surface and the film started to peel off from the Cr/Au micropattern after 10,000 cycles. These cracks are formed due to the structural degradation of PPy matrix because of volumetric swelling and shrinkage during cycling (Fig. S9, Supporting Information). The higher cycling stability of PPy@rGO can be ascribed to the mechanical flexibility of rGO, accommodating large volumetric changes and prevent structural pulverization. Furthermore, the PPy film deposited on Au is dense, whereas PPy on rGO has a highly porous network of PPy matrix. The results can be illustrated by nucleation mechanism, where wrinkled surface topology of rGO generates a promising background for the nucleation and electrochemical growth of nanoporous pseudocapacitive conducting polymers with improved interfacial contact and superior surface area.

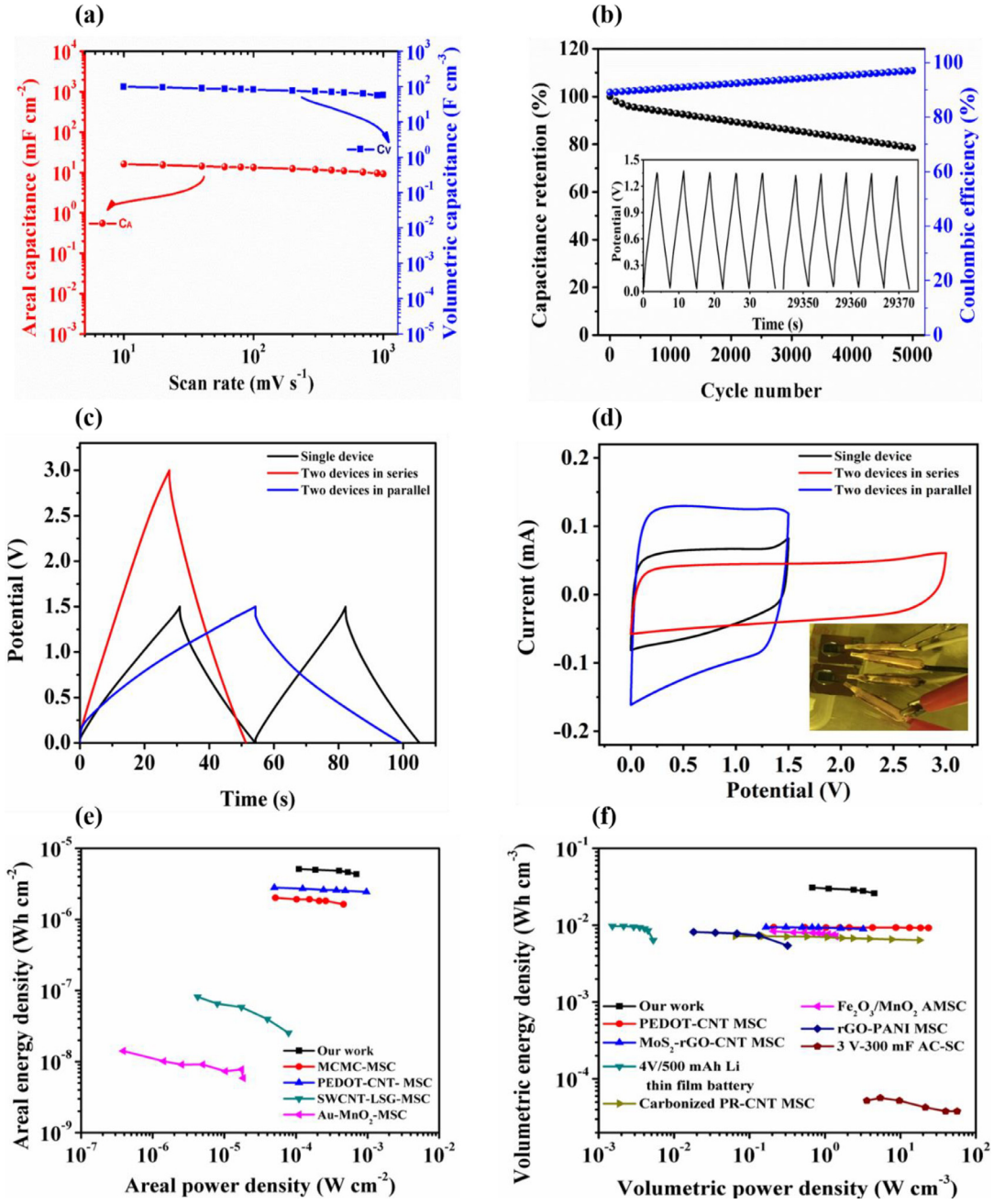

Fig. 5. (a) Scan rate vs. areal and volumetric specific capacitances of AMSC. (b) Cycling stability of AMSC measured at a very high current density of 10 mA cm^{-2} within a voltage window of 1.4 V, whereas the inset shows the initial 8 and last 8 cycles. (c) CV curves of single AMSC, series and parallel connected two MSCs at a scan rate of 50 mV s^{-1}. (d) GCD curves of single AMSC, series and parallel connected two MSCs at a current density of 1.0 mA cm^{-2}. (e) Ragone plots displaying areal energy and power densities of the fabricated MSCs compared with recently reported MSCs. (f) Volumetric energy and power densities of AMSC in comparison with recently reported MSCs.

3.1.2. Fabrication of stacking layered rGO-MSC

An rGO-based MSC was also fabricated by casting PVA/H_2SO_4 gel electrolyte on rGO microelectrodes. Fig. S8(a) shows the CV curves of rGO-MSC at different scan rates from 10 to 400 mV s^{-1}. The rectangular CV curves show a typical electric double layer charge storage mechanism of layered rGO. The linear escalation in current by scan rate shows the good rate performance of rGO-MSC. Fig. S8(b) shows the GCD curves of rGO-MSC at different current densities (from 10 to 1000 μA cm^{-2}). The increase in current density causes linear change in discharge time, revealing the idyllic charge storage behavior of rGO. The rGO-MSC delivered an areal capacitance of 360 μF cm^{-2}, around threefold higher compared with those of previously reported rGO-based MSCs [25–27].

3.1.3. Fabrication of asymmetric microsupercapacitor (AMSC)

To demonstrate the capacitance matching of PPy@rGO anode and PEDOT@rGO cathode, an all polymer-based AMSC was fabricated and characterized. PEDOT cathode was synthesized as reported in our previous work with minor modifications (experimental section) [49]. For PEDOT nanostructures deposited on rGO, the corresponding SEM images are shown in Fig. S3(b). For AMSC, the capacitance matching of microelectrodes is essential to achieve excellent electrochemical performance. By adjusting the deposition time, the capacitances of anode and cathode are matched. Fig. S9 shows the discharge curves of PPy@GO anode and PEDOT@rGO cathode (at a current density of 0.25 mA cm^{-2}), and the capacitance matching is obtained by using Eqs. (1)–(3) (Sup-

porting Information). CV and GCD tests of PEDOT@rGO cathode are performed in comparison with PEDOT@Au microelectrode (Fig. S11). From the CV curves, it is clear that the PEDOT@rGO microelectrode exhibits a higher capacitance compared with PEDOT@Au microelectrode. The enhanced capacitance is attributed to the growth of nanostructured porous PEDOT spheres on layered rGO.

To further investigate the practicability of microelectrodes, an aqueous AMSC was assembled with PEDOT@rGO cathode and PPy@rGO anode. The capacitances of PPy@rGO and PEDOT@rGO are matched at a scan rate of 30 mV s^{-1} (Fig. 4a) and a current density of 0.25 mA cm^{-2} (Fig. S10, Supplementary Information). PEDOT electrochemically polymerized on rGO current collector at a constant potential (0.9 V) for 250 s delivers the capacitance equal to the capacitance of PPy@rGO. Fig. 4(b and c) display the CV (at a scan rate of 50 mV s^{-1}) and GCD (at a current density of 1 mA cm^{-2}) curves of assembled AMSC with a working voltage window ranging from 0.6 to 1.5 V, manifesting that PEDOT@rGO//PPy@rGO AMSC is stable within this voltage in aqueous electrolyte. When voltage increases from 0.6 to 1.5 V (at a current density of 1 mA cm^{-2}), the areal capacitance increases from 12.6 to 14.7 mF cm^{-2}, mainly due to the increased redox reactions of the microelectrodes. Meanwhile, during long-term cycling up to 1.5 V, the cathode will suffer some H_2 evolution and cause electrode degradation, hence we tested our device up to 1.4 V.

Fig. 4(d) displays the CV curves of PEDOT@rGO//PPy@rGO AMSC at various scan rates (10–100 mV s^{-1}). The quasi-rectangular CV curves evidently show the typical capacitive performance and excellent reaction reversibility of AMSC. Additionally, the charge/discharge curves recorded at different current densities (from 0.25 to 2 mA cm^{-2}) display triangular profiles, confirming the excellent capacitive behavior of PEDOT@rGO//PPy@rGO AMSC (Fig. 4e). The maximum areal and volumetric capacitances of PEDOT@rGO//PPy@rGO AMSC are calculated as 15.9 mF cm^{-2} and 99.3 F cm^{-3} from charge/discharge curves at a current density of 0.25 mA cm^{-2}, significantly superior than those of previously reported planar MSCs, such as MnO_2//Fe_2O_3 AMSC [54], GQDS//MnO_2 [55], $Co(OH)_2$//erGO, PEDOT-CNT MSC [49], PEDOT MSC [30]. Further, the PEDOT@rGO//PPy@rGO-AMSC has an excellent rate capability of 78% at a high current density of 2 mA cm^{-2} (Fig. S12).

Fig. 4(f) displays the complex Nyquist plot (frequency range 0.01 Hz to 100 kHz) of PEDOT@rGO//PPy@rGO-AMSC. Overall resistance of the AMSC is calculated by the sum of effective series resistance (ESR) and equivalent distributed resistance (EDR) in high frequency region, which is about 296 ohm. ESR value of AMSC is also calculated from the voltage drop (IR) at the beginning of the galvanostatic discharge curve under a current density of 1.0 mA cm^{-2}, which is comparable with the ESR value obtained from EIS plot at high frequency region. In low frequency region, the EIS plot of PEDOT@rGO//PPy@rGO-AMSC is virtually parallel to the y-axis (imaginary axis) which justifies the perfect charge storage mechanism of the device.

To investigate the rate capability of AMSC, capacitance is plotted as function of scan rate and displayed in Fig. 5(a). By CV curves analysis, the specific areal (C_A) and volumetric capacitances (C_V) of PEDOT@rGO//PPy@rGO-AMSC are calculated as 16.2, 13.24, 10.87 mF cm^{-2} and 100.2, 82.75, and 67.95 F cm^{-3} respectively at scan rates of 10, 100, and 500 mV s^{-1}, demonstrating an excellent rate capability of 67.8%.

Fig. 5(b) shows the cycling performance and Coulombic efficiency of AMSC. PEDOT@rGO//PPy@rGO-AMSC retained 79% of the initial capacitance after 5000 charge/discharge cycles at a higher current density of 5 mA cm^{-2}. As the number of cycles increases, the active material becomes more penetrable and the electrolyte ionic resistance decreases and ultimately decreases in charge time, resulting in an increase in the Coulombic efficiency from 86% to 96% during 5000 cycles. To achieve the high voltage/specific capacitance, MSCs are always assembled in series or in parallel. CV and GCD results (Fig. 5c and d) display the discharge current and discharge time of two AMSCs in parallel combination is twofold compared with single device at constant voltage window. In the meantime, the obtained voltage of two AMSCs in series is almost twice. The results demonstrate that the fabricated AMSC has good compatibility and ultimately coped well in lieu of power applications. The high specific capacitance, excellent rate capability, and adjustable voltage window of AMSC will open the ways for all polymer-based AMSCs with applications in on-chip power source.

Ragone plots with the areal/volumetric energy and power densities for entire device are displayed in Fig. 5(e and f) (thickness of the microelectrode is 1.6 μm). The PEDOT@rGO//PPy@rGO-AMSC delivers volumetric energy densities of 27.12, 26.04, and 25.07 mWh cm^{-3} at power densities of 1.09, 2.17 and 3.26 W cm^{-3}, respectively (Fig. 5f). The maximal energy density of PEDOT@rGO//PPy@rGO-AMSC is higher than those of reported MSCs and AMSCs, such as PEDOT-CNT MSC [49], MnO_2/Fe_2O_3 AMSC [54], MoS_2-rGO-CNT MSC [11], laser scribed MoS_2 MSC [55], 3D Bicontinuous porous carbon MSC [56], Ni-Zn Microbattery [57], even higher than 4 V 500 mAh Li thin film battery [58] and 3V-300 mF AS-SC [59]. The areal energy density of PEDOT@rGO//PPy@rGO-AMSC is higher than those of many reported MSCs, as shown in Fig. 5(e). Further a detailed comparison of energy density of PEDOT@rGO//PPy@rGO-AMSC with aqueous batteries and conducting polymers-based MSCs is shown in Fig. S13. Finally, two AMSCs in series are demonstrated as an energy supply device to power a stopwatch (Fig. S14) for one minute after charging the MSCs at a current density of 0.5 mA cm^{-2}. Our approach provides a new way for micropatterning conducting polymers with great potential to develop all polymers-based aqueous MSCs, and reveals opportunities in wide range of microelectronic applications at high energy and power demands.

4. Conclusions

In summary, we fabricated a pseudocapacitive anode material based on PPy nonporous network anchored on electrochemically deposited multilayered rGO. The flexible nature of rGO on Au current collector accommodates high volume changes of PPy during successive charge/discharge cycles. Also the adhesion of PPy film with current collector is strengthened and offers high electrical conductivity. The PPy@rGO delivered excellent cycling stability maintaining 82% of the capacitance after 10,000 charge/discharge cycles in aqueous electrolyte at a higher current density. Moreover, the PEDOT@rGO cathode also showed enhanced electrochemical performance due to EDLC behavior of rGO and pseudocapacitive nature of polymer. The AMSC based on PPy@rGO anode and PEDOT@rGO cathode displayed a remarkable capacitive behavior, showing specific capacitances of 15.9 mF cm^{-2} (99.3 F cm^{-3}) and specific energy density of 4.3 μWh cm^{-2} (27.03 m Wh cm^{-3}) respectively at the voltage window of 1.4 V. Further, the aqueous AMSC showed an excellent cycling performance, retaining 79.2% of the initial capacitance after 5000 charge/discharge cycles at a higher current density of 5 mA cm^{-2}. Our study proposed a highly attractive strategy for facile fabrication of all polymer-based AMSCs with high electrochemical performance for on-chip electrochemical storage system.

Declaration of Competing Interest

None.

Acknowledgments

This work was supported by the National Natural Science Fund for Distinguished Young Scholars (51425204), the National Natural Science Foundation of China (51521001), the National Key Research and Development Program of China (2016YFA0202603, 2016YFA0202604), the Programme of Introducing Talents of Discipline to Universities (B17034), and the Yellow Crane Talent (Science & Technology) Program of Wuhan City.

Supplementary materials

Supplementary material associated with this article can be found, in the online version, at doi:10.1016/j.jechem.2020.02.036.

References

[1] N. Liu, W. Ma, J. Tao, X. Zhang, J. Su, L. Li, C. Yang, Y. Gao, D. Golberg, Y. Bando, Adv. Mater. 25 (2013) 4925–4931.
[2] S. Zhai, W. Jiang, L. Wei, H.E. Karahan, Y. Yuan, A.K. Ng, Y. Chen, Mater. Horiz. 2 (2015) 598–605.
[3] C. Zhang, M.P. Kremer, A. Seral-Ascaso, S.H. Park, N. McEvoy, B. Anasori, Y. Gogotsi, V. Nicolosi, Adv. Func. Mater. 28 (2018) 1705506.
[4] L. Mai, X. Tian, X. Xu, L. Chang, L. Xu, Chem. Rev. 114 (2014) 11828–11862.
[5] M. Beidaghi, Y. Gogotsi, Energ. Environ. Sci. 7 (2014) 867–884.
[6] M. Beidaghi, C. Wang, Adv. Funct. Mater. 22 (2012) 4501–4510.
[7] M.F. Elkady, R.B. Kaner, Nat. Commun. 4 (2013) 1475.
[8] Z.S. Wu, X. Feng, H.M. Cheng, Natl. Sci. Rev. 1 (2014) 277–292.
[9] L. Mai, X. Xu, C. Han, H. Luo, Y.Z. Xu, L. Wu, Y. Zhao, Nano Lett 11 (2011) 4992–4996.
[10] X. Shi, S. Pei, F. Zhou, W. Ren, M.H. Cheng, S.Z. Wu, X. Bao, Energy Environ. Sci. 12 (2019) 1534–1541.
[11] W. Yang, L. He, X. Tian, M. Yan, H. Yuan, X. Liao, J. Meng, Z. Hao, L. Mai, Small 13 (2017) 1700639.
[12] S. Wang, S.Z. Wu, S. Zheng, F. Zhou, C. Sun, M.H. Cheng, ACS Nano 11 (2017) 4283–4291.
[13] J. Chmiola, C. Largeot, P.L. Taberna, P. Simon, Y. Gogotsi, Science 328 (2010) 480–483.
[14] G. Lee, D. Kim, J. Yun, Y. Ko, J. Cho, J.S. Ha, Nanoscale 6 (2014) 9655–9664.
[15] W.A. Haider, M. Tahir, L. He, W. Yang, A. Minhas-khan, K.A. Owusu, Y. Chen, X. Hong, L. Mai, J Alloys Compd. 823 (2020) 151769.
[16] C. Zhang, H. Li, A. Huang, Q. Zhang, K. Rui, H. Lin, G. Sun, J. Zhu, H. Peng, W. Huan, Small 15 (2019) 1805493.
[17] S. Dai, H. Guo, M. Wang, J. Liu, G. Wang, C. Hu, Y. Xi, J. Mater. Chem. A 2 (2014) 19665–19669.
[18] L. Lang, Y. Dong, Y. Yao, L. Lin, W. Yue, Carbon 111 (2017) 121–127.
[19] X. Hong, L. He, X. Ma, W. Yang, L. Mai, Nano Res 10 (2017) 3743–3753.
[20] J. Chmiola, C. Largeot, P.L. Taberna, P. Simon, Y. Gogotsi, Science 328 (2010) 480–483.
[21] D. Pech, M. Brunet, H. Durou, P. Huang, V. Mochalin, Y. Gogotsi, P.L. Taberna, P. Simon, Nat. Nanotechnol. 5 (2010) 651–654.
[22] D. Pech, M. Brunet, P.L. Taberna, P. Simon, N. Fabre, F. Mesnilgrente, V. Conédéra, H. Durou, J. Power Sources 195 (2010) 1266–1269.
[23] M. Beidaghi, C.L. Wang, Adv. Func. Mater. 22 (2012) 4501–4510.
[24] J. Lin, C. Zhang, Z. Yan, Y. Zhu, Z. Peng, R.H. Hauge, D. Natelson, J.M. Tour, Nano Lett. 13 (2012) 72–78.
[25] K. Li, X. Liu, S. Chen, W. Pan, J. Zhang, J. Energy Chem. 32 (2019) 166–173.
[26] W. Gao, N. Singh, L. Song, Z. Liu, A.L.M. Reddy, L. Ci, R. Vajtai, Q. Zhang, B. Wei, P.M. Ajayan, Nature Nanotechnol. 6 (2011) 6–10.
[27] Z.S. Wu, K. Parvez, X. Feng, K. Müllen, Nat. Commun. 4 (2013) 2487.
[28] T.M. Dinh, K. Armstrong, D. Guay, D. Pech, J. Mater. Chem. A 2 (2014) 7170–7174.
[29] W. Si, C. Yan, Y. Chen, S. Oswald, L. Han, O.G. Schmidt, Energ. Environ. Sci. 6 (2013) 3218–3223.
[30] N. Kurra, N.A. Alhebshi, H.N. Alshareef, Adv. Energy Mater. 4 (2014) 1401303.
[31] K. Wang, W. Zou, B. Quan, H.Wu A.Yu, P. Jiang, Z. Wei, Adv. Energy Mater. 1 (2011) 1068–1072.
[32] C. Meng, J. Maeng, S.W.M. John, P.P. Irazoqui, Adv. Energy Mater. 4 (2014) 1301269.
[33] M. Beidaghi, C.L. Wang, Electrochim. Acta 56 (2011) 9508–9514.
[34] Z.S. Wu, G. Zhou, L.C. Yin, W. Ren, F. Li, H.M. Cheng, Nano Energy 1 (2012) 107–131.
[35] M. Zhi, C. Xiang, J. Li, M. Li, N. Wu, Nanoscale 5 (2013) 72–88.
[36] Q. Jiang, N. Kurra, H.N. Alshareef, Adv. Func. Mater. 25 (2015) 4976–4984.
[37] W. Liu, C. Lu, X. Wang, R.Y. Tay, B.K. Tay, ACS Nano 9 (2015) 1528–1542.
[38] Y.Q. Li, X.M. Shi, X.Y. Lang, Z. Wen, J.C. Li, Q. Jiang, Adv. Func. Mater. 26 (2016) 1830–1839.
[39] P. Zhang, F. Zhu, F. Wang, J. Wang, R. Dong, X. Zhuang, O.G. Schmidt, X. Feng, Adv. Mater. 29 (2016) 1604491–1604497.
[40] Y. Song, J. Xu, X. Liu, J. Power Sources 249 (2014) 48–58.
[41] M. Bai, T. Liu, F. Luan, Y. Li, X. Liu, J. Mater. Chem. A 2 (2014) 10882–10888.
[42] Y. Zhao, B. Liu, L. Pan, G. Yu, Energ. Environ. Sci. 6 (2013) 2856–2870.
[43] W. Zhang, X. Wen, S. Yang, Langmuir 19 (2003) 4420–4426.
[44] G. Yu, X. Xie, L. Pan, Z. Bao, Y. Cui, Nano Energy 2 (2013) 213–234.
[45] T.F. Otero, J.G. Martinez, Adv. Func. Mater. 23 (2013) 404–409.
[46] S. Biswas, L.T. Drzal, Chem. Mater. 22 (2010) 5667–5671.
[47] J. Zhang, X.S. Zhao, J. Phys. Chem. C 116 (2012) 5420–5426.
[48] Y. Song, T. Liu, X. Xu, D. Feng, Y. Li, X. Liu, Adv. Func. Mater. 25 (2015) 4626–4632.
[49] M. Tahir, L. He, W.A. Haider, W. Yang, X. Hong, Y. Guo, X. Pan, H. Tang, Y. Li, L. Mai, Nanoscale 11 (2019) 7761–7770.
[50] Z. Wang, C. Ma, H. Wang, Z. Liu, Z. Hao, J. Alloy. Compd. 552 (2013) 486–491.
[51] L.F. Chen, Z.-.Y. Yu, X. Ma, Z.-.Y. Li, S.-.H. Yu, Nano Energy 9 (2014) 345–354.
[52] M. Jayalakshmi, K. Bala subramanian, Int. J. Electrochem. Sci. 4 (2009) 878–883.
[53] S. Yumitori, J. Mater. Sci. 35 (2000) 139–146.
[54] Z. Liu, X. Tian, X. Xu, L. He, M. Yan, C. Han, Y. Li, W. Yang, L. Mai, Nano Res 10 (2017) 2471–2481.
[55] L. Cao S. Yang, W. Gao, Z. Liu, Y. Gong, L. Ma, G. Shi, S. Lei, Y. Zhang, S. Zhang, R. Vajtai, P.M. Ajayan, Small 9 (2013) 2905–2910.
[56] X. Ma, X. Hong, L. He, L. Xu, Y. Zhang, Z. Zhu, X. Pan, J. Zhu, L. Mai, ACS Appl. Mater. Interfaces. 11 (2019) 948–956.
[57] Z. Hao, L. Xu, Q. Liu, W. Yang, X. Liao, J. Meng, X. Hong, L. He, L. Mai, Adv. Func. Mater. 29 (2019) 1808470.
[58] B. Shen, J. Lang, R. Guo, X. Zhang, X. Yan, ACS Appl. Mater. Interfaces 7 (2015) 25378.
[59] M.F. El-Kady, M. Ihns, M. Li, J.Y. Hwang, M.F. Mousavi, L. Chaney, A.T. Lech, R.B. Kaner, Proc. Natl. Acad. Sci. U. S. A. 112 (2015) 4233–4238.